Materialia 000 (2020) 100543

Contents lists available at ScienceDirect

Materialia

journal homepage: www.elsevier.com/locate/mtla

Full Length Article

Towards dynamic tension-compression asymmetry and relative deformation mechanisms in magnesium

C. Kale[a], S. Turnage[a], D.Z. Avery[b], H. El Kadiri[c], J.B. Jordon[b], K.N. Solanki[a,*]

[a] School for Engineering of Matter, Transport and Energy, Arizona State University, Tempe, AZ, USA
[b] Department of Mechanical Engineering, University of Alabama, Tuscaloosa, AL, USA
[c] Department of Mechanical Engineering, Mississippi State University, Starkville, MS, USA

ARTICLE INFO

Keywords:
Dynamic behavior
Split Hopkinson pressure bar
Tension-compression asymmetry
Twinning

ABSTRACT

We present the first results of high-rate tension followed by compressive loading on a textured AZ31 alloy using a novel split-Hopkinson-pressure-bar (SHPB). The traditional-SHPB was modified in order to apply tension followed by compression along the rolling direction within few millisecond differences and a strain-rate of 10^3 s^{-1}. The initial and post-deformed microstructure was examined by electron backscatter diffraction. The results reveal a reduced tension–compression asymmetry along with a shallower than the traditional sigmoidal-curve, indicating a significant influence of forward tensile loading on the subsequent compression behavior, manifested by the role of adiabatic-heating along with some unique deformation behavior.

1. Introduction

Mechanical properties are well established for a wide range of structural materials under certain loading conditions such as uniaxial-load, low strain-rates, and isentropic environments [1]. However, in practical application, structural materials experience complicated loading environment conditions such as high strain-rates, multi-directional loading states, and adiabatic thermal conditions. In particular, load reversal can cause a dramatic change in mechanical behavior due to microstructural changes during the forward loading [2]. For instance, in wrought Mg alloys, such as AZ31 alloy, a strong basal texture is developed during the rolling process, which leads to high tension-compression anisotropy at room temperature irrespective of the deformation rate [3,4]. This classic anisotropy is due to the dependence of the relative activity of various deformation modes having quite distinct critical resolved shear stresses (CRSS) on the loading direction [5–8]. For example, in the case of in-place compression (e.g. along the rolling direction - RD), $\{10\bar{1}2\}$ extension twinning is profuse, resulting into a relatively low yield strength and a sigmoidal stress – strain behavior characteristic of a rapid hardening regime [3]. However, tensile deformation along the RD is mainly accommodated by prismatic and basal slip with little contribution from twinning, which leads to a parabolic stress-strain behavior [4] and a higher yield strength compared to in-plane compression. This asymmetric yield strength behavior has been well documented in literature for various strain-rate regimes [4,5,9,10], which is exacerbated as strain-rate increases or temperature decreases. However, there are still many unanswered questions regarding the effect of prior slip on the asymmetric behavior including adiabatic shear banding and ensuing heating. In fact, classical studies by Venables [11] concluding twinning stress has a parabolic dependence on the stacking-fault energy has been continuously challenged by several authors (e.g. [12]) whereupon the dislocation density and the homogeneous slip length have been demonstrated to be the most relevant microstructural variables that directly influence the twinning-stress in the polycrystal. For hcp crystal structures, increasing in the basal dislocation density can significantly influence twinning stress (i.e., twin growth behavior) [6]. Furthermore, the influence of strain-rate and reversed loading on the anisotropic behavior has not been properly addressed.

To fill this gap this, a novel Split Hopkinson pressure bar (SHPB) setup was used to study the effect of high rate tensile loading immediately followed by compressive loading, on a wrought AZ31 alloy with a basal (0002) texture. To date, only limited research has been performed to analyze the reverse loading effect in materials at high strain-rates. Early work by Nevill and Myers [13] used drop load testing to apply a preload in high purity aluminum followed by drop load testing in a reversed direction. Their results show that when compressive preload was applied first followed by tensile drop test, the yield strength anisotropy increases at strain-rates $>10^2$ s^{-1}. However, as Nevill and Myers point out, samples were allowed to recover from any time dependent effects from preloading such as adiabatic heating. In an effort to limit the time for specimen recovery, Peirs et al. [14] developed a torsional Kolsky bar which allowed reflection of a torsional wave such that the first and

* Corresponding author.
E-mail address: kiran.solanki@asu.edu (K.N. Solanki).

https://doi.org/10.1016/j.mtla.2019.100543
Received 18 September 2019; Accepted 24 November 2019
Available online xxx

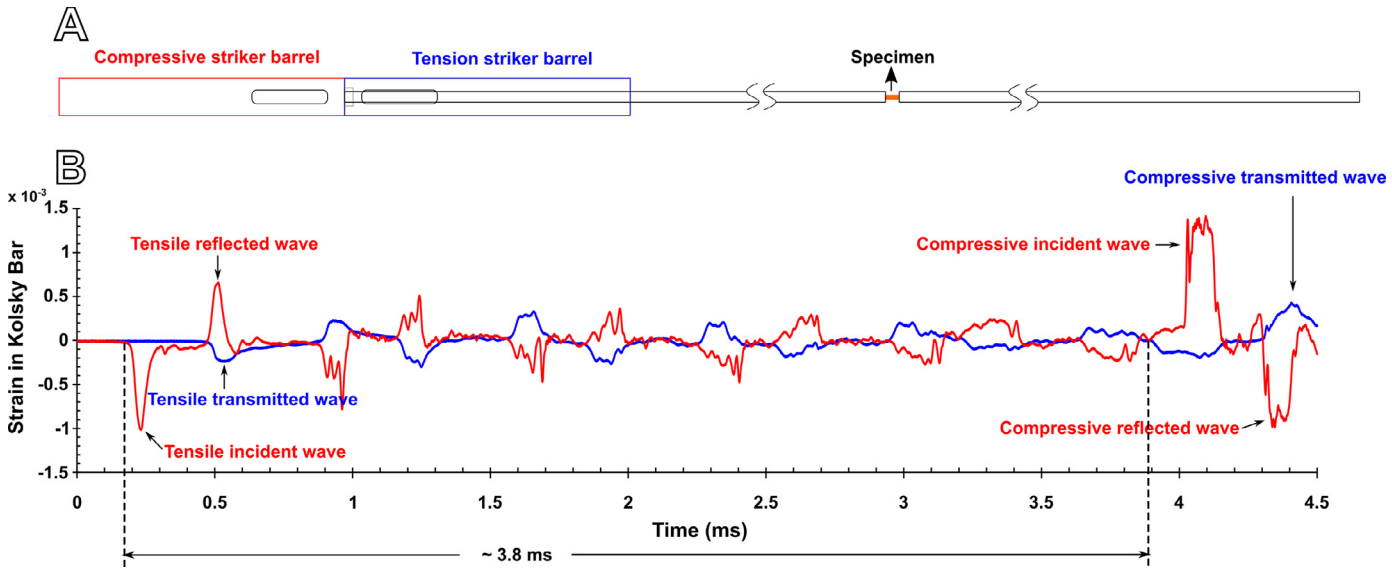

Fig. 1. (A) Schematic of the modified SHPB used for achieving tension followed by immediate compression loading. (B) Strain signals from the Kolsky bar plotted against time that indicate tensile preload can easily be distinguished from a compressive load which follows within ~3.8 ms time delay.

second torsional waves impacted the specimen in opposing directions. By comparing with quasi-static results, they showed that the torsional reversed load effect in Ti–6Al–4V is strain-rate dependent. Similarly, Nemat-Nasser et al. [15] used momentum trapping techniques to reverse a uniaxial Kolsky pulse to allow immediate reversal of the strain, but this technique has been shown to have a difference in strain-rates between forward and reversed loading of around 10^3 s^{-1}, which is significant for certain strain-rate sensitive materials [16]. Thus, in this work the conventional SHPB [17,18] was modified such that the forward and the reverse loading had comparable strain rates and forward tensile loading was instantaneously followed (within a few milliseconds) by a reverse compressive loading along the same sample orientation (to include adiabatic heating effects).

2. Experimental procedure

Fig. 1A illustrates the novel setup of the SHPB, which was used in this work to obtain immediate reverse loading (tension followed by compression) at similar strain-rates. The incident and the transmitted bar was made out of Al7075 and hade a diameter of 0.5 in., respectively. The tension and the compression barrels were butted against each other such that the incident bar for both the loadings is same. The respective strikers in tension and compression barrel are propelled by the sudden release of compressed nitrogen gas through simultaneous actuation of two independent solenoid valves connected in a parallel circuit. The time delay between the start of the incident tensile wave and the incident compression wave was adjusted by careful positioning of the impact end of the incident bar such that the tensile striker hits first shortly followed by the compression striker. The position of the impact end of the incident bar was chosen by trial and error method in order to obtain a bare minimum time delay (of a couple of milliseconds) between the start of each incident wave.

A representative wave diagram from a test for which a delay of 3.8 ms occurred can be found in Fig. 1B. Following such a test, strain-gauge signals for tension and compression are analyzed separately using the methods outlined in [19–21] and are in turn used to calculate the stress–strain curve of the material being tested. In this work, the effect of tension followed by compression loading was studied in a hot rolled AZ31 plate under two conditions – (1) the forward tensile loading was followed by the reverse compression loading with a time delay of 3 h; and (2) the forward tensile load was immediately followed by the reverse compression load with a few milliseconds of time delay. Multiple tests were performed for different testing scenarios and in each case the forward and the reverse load was applied along the same loading axis. The loading axis was kept parallel to the RD of the hot rolled AZ31 plate for all experiments within this study. Individual mechanical behavior along the RD under uniaxial tension and compression loading respectively was characterized earlier (see Supplemental document in [9]) for the same material. Cylindrical dog-bone samples with a gage diameter of 3.25 mm and gage length of 3.25 mm were used for all loading scenarios.

The as-received and the post-deformed microstructure was analyzed using electron backscatter diffraction (EBSD) characterization. For post-deformed characterization, the samples were carefully prepared from the middle of the gage section and the viewing direction was aligned along the loading direction. Moreover, multiple samples were analyzed in order to cover most of the gage area. Sample preparation for EBSD included mechanical grinding to flatten the sample to upwards of 1200 grit SiC paper with ethanol as lubricant. Mechanical grinding was followed by electropolishing using Struers LectroPol 5 polisher operated at 22 V for 20 s and an electrolyte flow rate of 12. C1 electrolyte was used which consisted of 160 g sodium thiocyanate, 800 ml ethanol, 80 ml ethylene glycol monobutyl ether, and 20 ml distilled water. The electrolyte was stored in a lab freezer overnight before using. EBSD characterization was performed using a Tescan Lyra FIB-FESEM, coupled with an EDAX Hikari Super EBSD camera. EBSD experiments were performed at an acceleration voltage of 15 keV and with a scan step size of 0.6 μm. The data was analyzed using a TSL OIM software and a Neighbor CI Correlation algorithm was used for cleaning of the data set. A CI index of 0.2 was used for one iteration and a total of three iterations were performed.

3. Results and discussion

Fig. 2A below represents the EBSD scan along the plane perpendicular to the normal direction (ND) of the as-received hot rolled AZ31 plate. The average grain size in the as-received condition was calculated to be around 15 ± 2 μm (calculated over 400–500 grains). Basal (0002) pole figure along the plane perpendicular to the ND, Fig. 2B, indicates that the as-received plate has a strong basal texture closely aligned parallel with the ND of the plate. Further details on the as-received microstructure characterization can be found in the supplemental document in

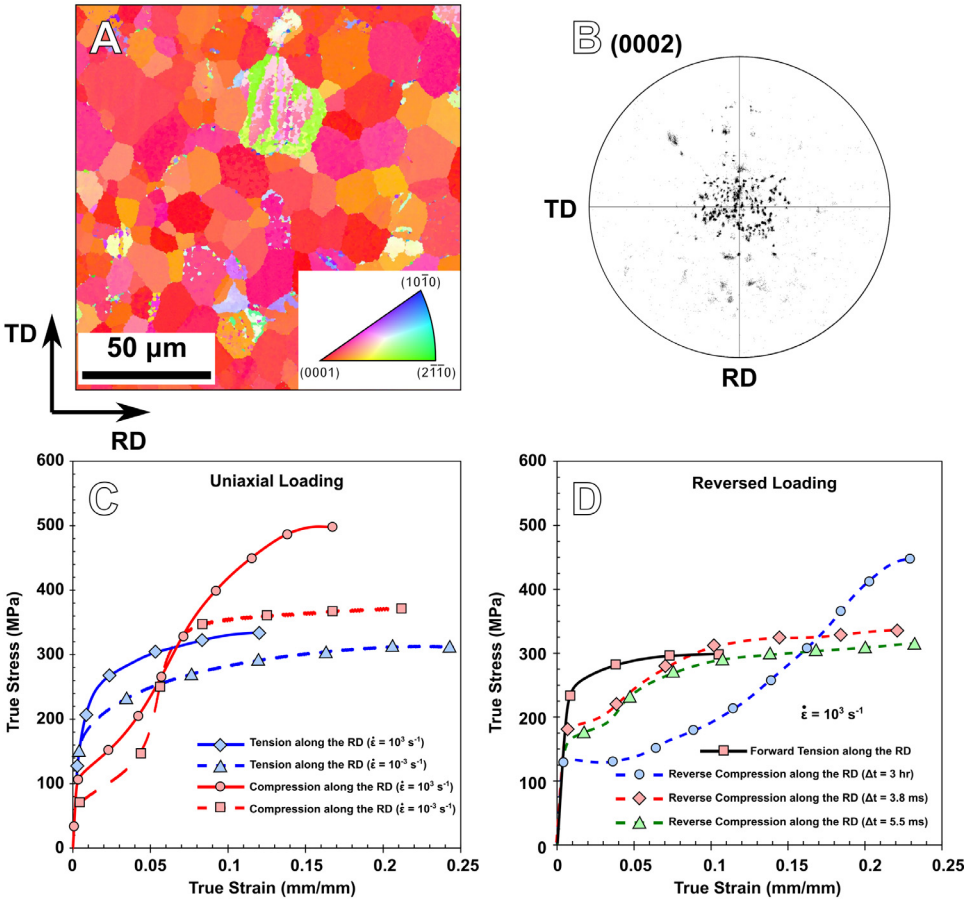

Fig. 2. (A) As-received EBSD scan for the hot rolled AZ31 plate along the plane perpendicular to the ND. (B) Basal (0002) pole figures obtained along the plane perpendicular to the ND for the sample in (A). (C) True stress–true strain curves along the RD for pure uniaxial loading at different strain-rates. (D) True stress–true strain curves along the RD for reversed loading for three different time delays and at high strain-rate (10^3 s^{-1}).

[9]. First, the uniaxial tensile and compressive flow stress behavior, subjected to both quasi-static (10^{-3} s^{-1}) and dynamic ($\geq 10^3$ s^{-1}) strain-rate, along the RD is plotted in Fig. 2C. Compression loading along the RD at both strain-rates (solid and dashed red lines in Fig. 2C) results in a sigmoidal stress–strain curve similar to previously published literature [22–25]. Such sigmoidal curve indicates the influence of twinning deformation mechanism. For AZ31 with a strong basal (0001) texture along the ND, compression loading along the RD is favorably oriented for the activation of {10$\bar{1}$2} extension twinning deformation mode [26–30]. For tensile loading along the RD, the deformation occurs via dislocation slip and the stress–strain curve has a more conventional appearance for both strain-rates (solid and dashed blue lines in Fig. 2C). The activation of different types of deformation modes under different types of uniaxial loading, results in an inherent yield strength asymmetry for wrought AZ31 alloy. There is a difference in the yield strength of about ~40% for tensile and compression loading along the RD for this material. In this work, we try to identify the influence of forward tensile loading along the RD on the reverse compressive behavior at dynamic strain-rates (10^3 s^{-1}), again along the RD, as a function of different time delays between the forward tensile and reverse compression loading.

Fig. 2D above represents the true stress–true strain response in case of reversed loading at dynamic strain-rates along the RD and for two time delays several orders of magnitude apart (3.8 ms and 5.5 ms versus 3 h). Solid black curve in Fig. 2D is a representative curve for three different forward tensile loadings obtained along the RD and similar strain-rates (couple of hundreds difference). The red and the green curve show the behavior under reversed compression loading with a time delay of 3.8 ms and 5.5 ms, respectively and the blue curve corresponds to the time delay of 3 h. From the plot in Fig. 2D, it can be clearly seen that the true stress–true strain behavior under reverse compression loading clearly depends on the time delay between the forward and the reverse loading. For comparable strain-rates, the yield strength in the case of the samples with instantaneous reverse loading (3.8 ms and 5.5 ms) is higher as compared to the sample with the prolonged time delay (3 h). Moreover, the sigmoidal nature of the true stress–true strain curve is steeper in the case of instantaneously reversed samples. This clearly indicates a major influence of the forward tensile loading along the RD on the reverse compressive behavior along the same orientation at dynamic strain-rates. Table 1 provides a more quantitative analysis of the results presented in Fig. 2D.

Table 1
Yield strength at quasi-static strain-rates (10^{-3} s^{-1}), 1% and 5% flow stress at high strain-rate (10^3 s^{-1}) under various loading conditions along the RD.

	Yield strength at 10^{-3} s^{-1} (MPa)	1% Flow stress at 10^3 s^{-1} (MPa)	5% Flow stress at 10^3 s^{-1} (MPa)
Uniaxial Compression	75	127	261
Uniaxial Tension	169	246	301
Forward Tension	–	250	280
Reversed compression with 3 h delay	–	130	140
Reversed compression with 5.5 ms delay	–	168	237
Reversed compression with 3.8 ms delay	–	185	248

Table 1 provides the 0.2% yield strength in case of quasi-static rate (10^{-3} s^{-1}) and 1% and 5% flow strength in case of dynamic rate (10^3 s^{-1}) for various loading conditions along the RD of the AZ31 plate. For understanding the influence of forward tensile loading, we will compare the 1% and 5% compressive flow strength in case of reverse compression loading having different time delays with the respective compressive flow strength of uniaxial compression loading for similar strain-rates.

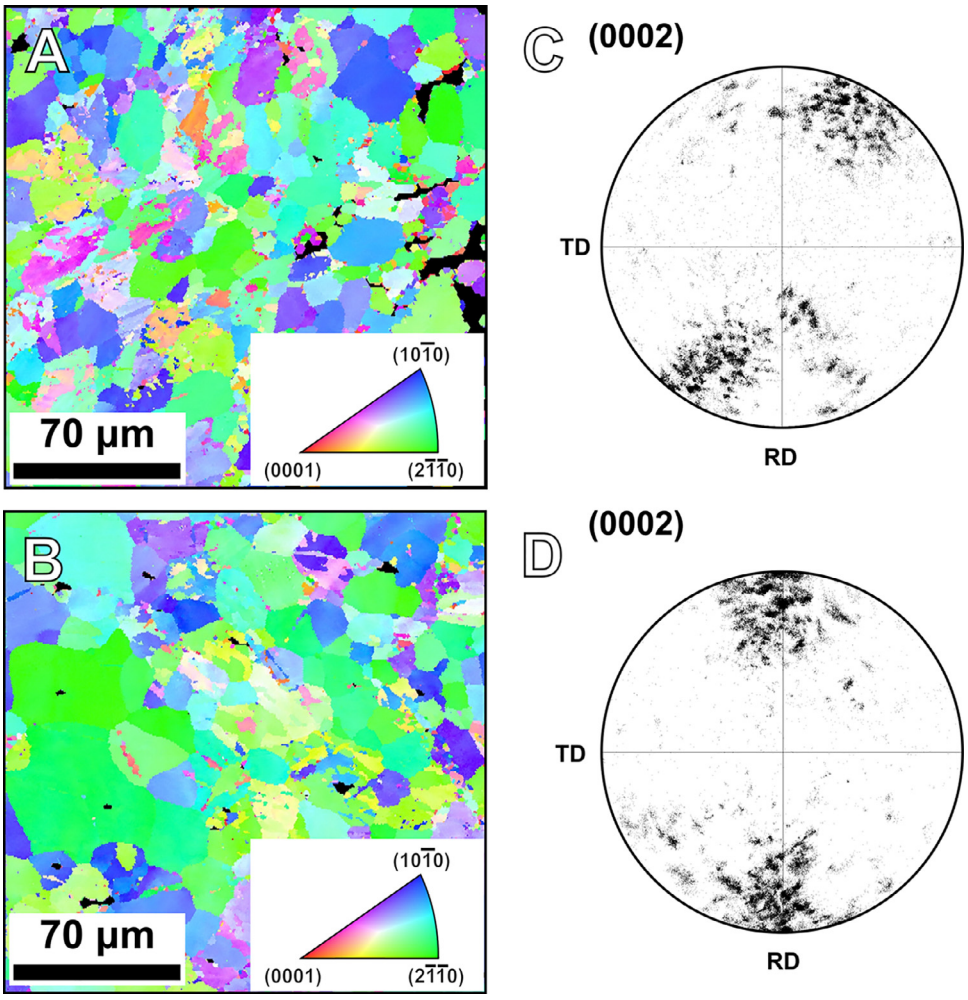

Fig. 3. Post-deformed EBSD analyses with the plane of view perpendicular to the RD (but the crystallographic data were rotated such that ND became normal to the plane of the paper) showing (A) an inverse pole figure and (C) corresponding (0002) pole figure of a sample reverse loaded with a time delay of 3.8 ms, (B) an inverse pole figure and (D) (0002) pole figure of a sample reverse loaded with a time delay of 3 h, respectively.

Note that in SHPB experiments, equilibrium of the stress waves inside the specimen needs to be attained and thus it is relatively difficult to measure the true yield strength under such conditions. As such, the comparison will be fousced on 1% and 5% compressive flow strength. Let us first consider the reverse loading condition with 3hr time delay, the 1% flow strength (130 MPa) compares well with the 1% flow strength (127 MPa) in case of uniaxial compression loading. However, the 5% flow strength (140 MPa) for the same loading scenario is almost 50% less compared to the uniaxial loading (261 MPa). This indicates that the rate of strain hardening post yield (due to twinning) for reverse compression loading having 3 h time delay is much slower compared to the uniaxial compression loading. Next, let us consider the two cases where the reverse loading was almost instantaneous (3.8 ms and 5.5 ms). The average 1% flow strength (average of 168 MPa and 185 MPa) is almost 50% higher compared to the uniaxial loading condition (127 MPa). However, the avergae 5% flow strength (average of 237 MPa and 248 MPa) is comparable to the 5% flow strength of uniaxial loading (261 MPa). This indicates that the rate of strain hardening post yield in case of instantaneous reverse compression laoding is similar to the uniaxial compression loading. Finally, another important observation is related to the saturation stress, i.e., for the 3.8 ms/5.5 ms delay cases, the saturation stress was found to be lower as compared to other conditions. It can be concluded that the forward tensile loading combined with the time delay between the reverse compression loading and strain-rates have a major influence on the flow strength and the rate of strain hardening of the reverse compression loading. In the next sections we will try to address this influence on the post-deformed microstructure as well as discuss the reason for this influence.

Fig. 3 provides the microstructural orientation information through EBSD analysis of the samples tested under various high rate conditions along the RD. The EBSD maps (Fig. 3A and B) and corresponding pole figures (Fig. 3C and D) were obtained from the middle of the gage section for all test conditions. The microstructure and texture evolution during high strain-rate deformation for the reverse loaded with a time delay of 3.8 ms and 3 h, show similar behavior. However, the average compressive 1% flow strength (average of 168 MPa) for a time delay of 3.8 ms is almost 50% higher compared to sample that was reversed loaded with a time delay of 3 h. To explain such behavior, first we perform adiabatic heating analysis [31] to calculate the temperature rise (ΔT) for the instantaneously reversed samples with 3.8/5.5 ms delay using the following generic form

$$\Delta T(\varepsilon) = \frac{\eta}{\rho C_v}\int_0^{\varepsilon} \sigma \, d\varepsilon \tag{1}$$

where σ is the true stress, ε is the true strain, ρ is the density of the material, η is the efficiency factor, which is assumed to be 1 (see [31,32]), C_v is the specific heat capacity at constant volume. For a 10% forward tensile loading, the temperature rise was calculated to be about 15 °C, i.e., the overall temperature within the sample would be around 40 °C. However, AZ31 has a high tendency to deform locally, so a global strain of 10% can account for up to localized strains of about 30% within the sample with a large strain gradient. This being said, the adiabatic temperature rise being a function of the total strain (Eq. (1)), the regions which experience strain localization would see a higher temperature rise (total temperature could roughly be around 70 °C). Time delay of 3.8 ms

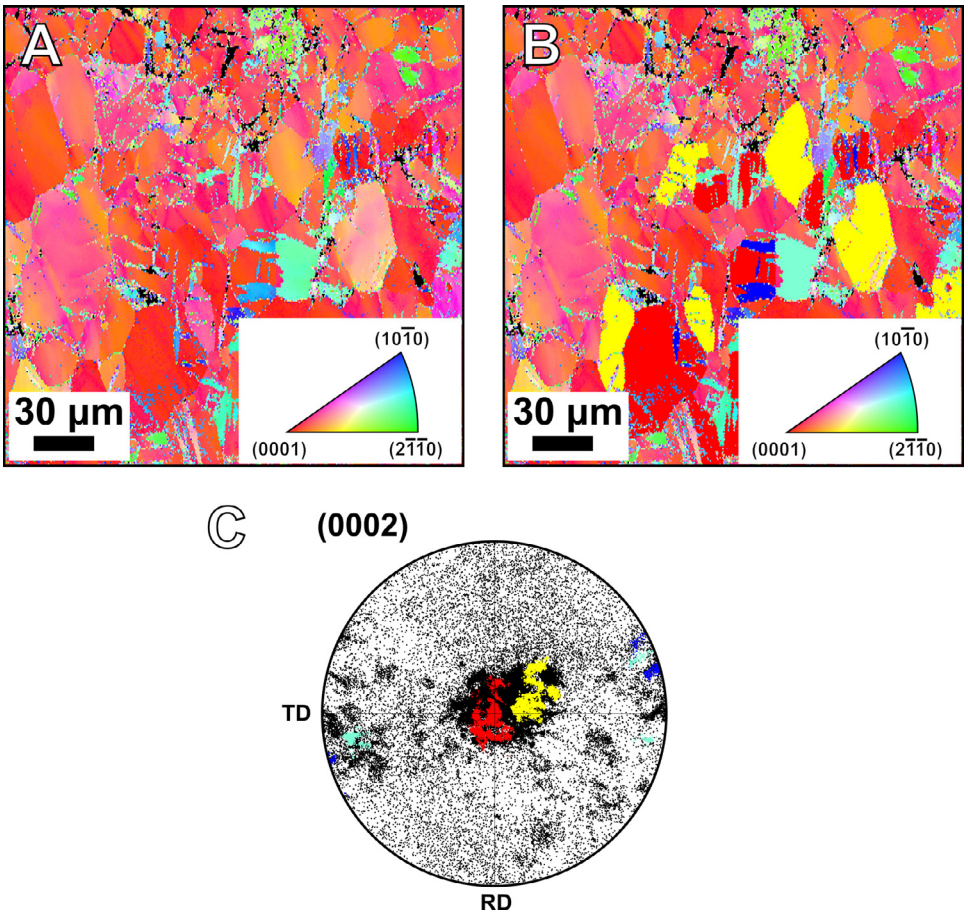

Fig. 4. Post-deformed EBSD analysis of a sample tested at high strain rate (10^3 s^{-1}) under in-plane uniaxial tension with the plane of view perpendicular to the RD (but the crystallographic data were rotated such that ND became normal to the plane of the paper) showing (A) an inverse pole figure (IPF) with (B) the same IPF as in (A) but the grains who have not twinned are highlighted in yellow (not related to the IPF color scheme) while the grains who have twinned are highlighted in red (not related to the IPF color scheme), and the twins are highlighted in green and blue. (C) Their corresponding pole figure (PF) showing the crystallographic location of the highlighted grains and twins in the inverse pole figure.

or 5.5 ms are typically not enough to dissipate the heat generated for a bulk sample and as a result deformation via slip is promoted at the onset of yielding during instantaneous load reversal. Thus, the higher 1% flow stress in the case of reversed compression loading for 3.8 ms and 5.5 ms case compared to the 3 h time delay clearly can be explained by the higher contribution of slip at the onset of plasticity. As twinning is athermal, the increase in slip activity limits the activity of twinning but does not eliminate, as the rise in temperature is still insufficient to do so. In particular, the increased slip activity suppresses more twin nucleation than twin propagation. In fact, twin nucleation mostly occurs at the onset of plasticity, at the time when the CRSSs of slip modes is still in early stage of hardening, while twin propagation operates at higher strain levels at which point the CRSSs have increased high enough to allow twinning dominated plasticity. Though fewer twins are expected in these conditions, they would still grow and invade the whole parent grains. Invasion of the parent grains by the {10$\bar{1}$2} extension twins is associated with a ~86° grain rotation and texture realignment. This can be confirmed by comparing the basal (0002) pole figures in the post-deformed condition (Fig. 3B and D) and in the as-received condition (Fig. 2B).

This explanation reconciles the combination of a sigmoidal shape (similar twin propagation rate) and a lower saturation stress (lower twin nucleation rate) of the stress-strain curves in the instantaneously reversed samples (3.8 ms and 5.5 ms time delay) compared to the 3 h time delay condition. El Kadiri and Oppedal [33] and Oppedal et al. [34,35] demonstrated that the difference in saturation stress between the sigmoidal curve and the parabolic curve retrieved whether by strain path or stress sign reversal is mainly driven by the contribution of dislocation transmutation to hardening. This is consistent with the fact that dislocation transmutation is expected to be more noticeable in the case of higher twin nucleation. Overall, the effect of adiabatic heating due to local strain gradients correlated well with observed saturation stress, high yield, and hardening rates.

Next, we address an another important observation from this work that is related to the strain-rate effects on twinning under forward in-plane tensile loading through Fig. 4. In magnesium and its alloys, extension {10$\bar{1}$2} twinning has been widely reported to be completely absent until now when a basal texture is stretched normal to the fiber axis (in-plane). However, results in Fig. 4 reveal the opposite under high-rate conditions. As evident from the pole figure (PF) in Fig. 4C, grains highlighted in red and yellow colors lie nearby on the PF and have their c-axis closely aligned with the ND of the plate. Such grain orientations are not favorable for extension {10$\bar{1}$2} twinning under in-plane tension and hence, their Schmid's factor is nearly zero for the respective deformation mode. Thus from Fig. 4B and C, it can be seen that many grains (highlighted by red color) with nearly zero Schmid's factor have experienced noticeable twinning, while others (highlighted by yellow color) with similar Schmid's factor behaved as expected showing no twinning. Furthermore, most of grain boundaries regardless whether surrounding grains have twinned or not are intermittently decorated by {10$\bar{1}$2} micro twins. These non-Schmid's phenomena could be attributed to the fact that at high strain-rates, the CRSS of non-basal slip nearby grain boundaries becomes so high that it triggers mechanisms promoting {10$\bar{1}$2} twin nucleation from non-basal slip stacking faults [6]. This behavior shows the dramatic effect of high strain-rate on hardening slip and thus giving a substantial opportunity for twins to nucleate but grow in a limited fashion.

4. Conclusion

In summary, we present the first results of high-rate tension followed by compressive loading on a textured AZ31 alloy using a novel SHPB setup. The results reveal a reduced tension–compression asymmetry along with a shallower than the traditional sigmoidal curve at high-rate, indicating a significant influence of forward tensile loading on the subsequent compression behavior, and suggesting a role of adiabatic heating on the mechanical response of AZ31 alloy under immediate reverse loading. Of considerable importance is the substantial grain boundary nucleation of $\{10\bar{1}2\}$ twins in unfavorably oriented grains under high rate conditions. This shows the drastic effect of rate dependence of slip on twinning, which is not properly captured yet in crystal plasticity simulation modeling.

Declaration of Competing Interest

None.

Acknowledgments

The authors would like to thank the National Science Foundation (grant number 1554632) for their financial assistance.

Supplementary material

Supplementary material associated with this article can be found, in the online version, at doi:10.1016/j.mtla.2019.100543.

References

[1] M.A. Meyers, K.K. chawla, Mechanical Behavior Materials, Cambridge University Press, United Kingdom, 2008.
[2] J.B. Jordon, M.F. Horstemeyer, K. Solanki, J.D. Bernard, J.T. Berry, T.N. Williams, Mater. Sci. Eng. A 527 (2009) 169–178.
[3] M.T. Tucker, M.F. Horstemeyer, P.M. Gullett, H. El Kadiri, W.R. Whittington, Scr. Mater. 60 (2009) 182–185.
[4] I. Ulacia, N.V. Dudamell, F. Gálvez, S. Yi, M.T. Pérez-Prado, I. Hurtado, Acta Mater. 58 (2010) 2988–2998.
[5] S.R. Agnew, Ö. Duygulu, Int. J. Plast. 21 (2005) 1161–1193.
[6] F. Wang, C.D. Barrett, R.J. McCabe, H. El Kadiri, L. Capolungo, S.R. Agnew, Acta Mater. 165 (2019) 471–485.
[7] J.W. Christian, S. Mahajan, Prog. Mater. Sci. 39 (1995) 1–157.
[8] P. Garg, I. Adlakha, K.N. Solanki, Acta Mater. 153 (2018) 327–335.
[9] C. Kale, M. Rajagopalan, S. Turnage, B. Hornbuckle, K. Darling, S. Mathaudhu, K. Solanki, Mater. Res. Lett. 6 (2018) 152–158.
[10] D.L. Yin, J.T. Wang, J.Q. Liu, X. Zhao, J. Alloys Compd. 478 (2009) 789–795.
[11] J.A. Venables, J. Phys. Chem. Solids 25 (1964) 693–700.
[12] E. El-Danaf, S.R. Kalidindi, R.D. Doherty, Metall. Mater. Trans. A 30 (1999) 1223–1233.
[13] G.E. Nevill Jr., C.D. Myers, J. Mech. Phys. Solids 16 (1968) 187–194.
[14] J. Peirs, P. Verleysen, J. Degrieck, EPJ Web Conf. 26 (2012) 01023.
[15] S. Nemat-Nasser, J.B. Isaacs, J.E. Starrett, Proc. R. Soc. Lond. Ser. Math. Phys. Sci. 435 (1991) 371–391.
[16] B. Song, W. Chen, Exp. Mech. 44 (2004) 622–627.
[17] H. Kolsky, Proc. Phys. Soc. Sect. B 62 (1949) 676.
[18] W.W. Chen, B. Song, Split Hopkinson (Kolsky) Bar: Design, Testing and Applications, Springer, 2010.
[19] B.A. Gama, S.L. Lopatnikov, J.Gillespie John W, Appl. Mech. Rev. 57 (2004) 223–250.
[20] D.J. Barton, C. Kale, B.C. Hornbuckle, K.A. Darling, K.N. Solanki, G.B. Thompson, Mater. Sci. Eng. A 725 (2018) 503–509.
[21] S.A. Turnage, M. Rajagopalan, K.A. Darling, P. Garg, C. Kale, B.G. Bazehhour, I. Adlakha, B.C. Hornbuckle, C.L. Williams, P. Peralta, K.N. Solanki, Nat. Commun. 9 (2018) 2699.
[22] F. Kabirian, A.S. Khan, T. Gnäupel-Herlod, Int. J. Plast. 68 (2015) 1–20.
[23] A. Staroselsky, L. Anand, Int. J. Plast. 19 (2003) 1843–1864.
[24] H. Wang, P.D. Wu, J. Wang, C.N. Tomé, Int. J. Plast. 49 (2013) 36–52.
[25] X. Yu, Y. Li, Q. Wei, Y. Guo, T. Suo, F. Zhao, Mech. Mater. 86 (2015) 55–70.
[26] N.V. Dudamell, I. Ulacia, F. Gálvez, S. Yi, J. Bohlen, D. Letzig, I. Hurtado, M.T. Pérez-Prado, Acta Mater. 59 (2011) 6949–6962.
[27] X.Y. Lou, M. Li, R.K. Boger, S.R. Agnew, R.H. Wagoner, Int. J. Plast. 23 (2007) 44–86.
[28] O. Muránsky, D.G. Carr, P. Šittner, E.C. Oliver, Int. J. Plast. 25 (2009) 1107–1127.
[29] A. Pandey, F. Kabirian, J.-.H. Hwang, S.-.H. Choi, A.S. Khan, Int. J. Plast. 68 (2015) 111–131.
[30] R. Reed-Hill, The Inhomogeneity of Plastic Deformation, AMS, Materials Park, OH, 1973.
[31] R. Kapoor, S. Nemat-Nasser, Mech. Mater. 27 (1998) 1–12.
[32] D. Ghosh, O.T. Kingstedt, G. Ravichandran, Metall. Mater. Trans. A 48 (2017) 14–19.
[33] H. El Kadiri, A. Oppedal, J. Mech. Phys. Solids 58 (2010) 613–624.
[34] A. Oppedal, H. El Kadiri, C. Tomé, S.C. Vogel, M. Horstemeyer, Philos. Mag. 93 (2013) 4311–4330.
[35] A. Oppedal, H. El Kadiri, C. Tomé, G. Kaschner, S.C. Vogel, J. Baird, M. Horstemeyer, Int. J. Plast. 30 (2012) 41–61.